9 The $\pi^+ \to e^+\nu_e$ / $\pi^+ \to \mu^+\nu_\mu$ branching ratio

P. Robmann, A. van der Schaaf and P. Truöl

in collaboration with University of Virginia, Charlottesville, USA; Institute for Nuclear Studies, Swierk, Poland; JINR, Dubna, Russia; PSI, Villigen, Switzerland and Rudjer Bošković Intitute, Zagreb, Croatia

(PEN Collaboration)

Charged pions decay weakly into lepton pairs, $l_i\nu_i$, of the lower two generations ($i = 1, 2$) through an intermediate W boson. As discussed in some detail in last years' report, the ratio between the partial decay rates for $\pi^+ \to e^+\nu_e$ and $\pi^+ \to \mu^+\nu_\mu$ depends primarily on the masses of the particles involved:

$$R^{\pi}_{e/\mu} \equiv \frac{\Gamma(\pi \to e\nu_e)}{\Gamma(\pi \to \mu\nu_\mu)} \simeq \left(\frac{m_e}{m_\mu} \times \frac{m_\pi - m_\mu}{m_\pi} \times \frac{g_e}{g_\mu}\right)^2 ,$$

where g_i denotes the coupling strength of the $Wl_i\nu_i$ vertex ($g_e = g_\mu$ in the Standard Model). One readily identifies the factors associated with the helicity suppression, the Q-value, and the universality violation. Table 9.1 compares the theoretical value including all bells and whistles, which is a few percent below the above simple estimate, with the two-decades old experimental one. This comparison still gives the best constraint on a flavour dependent coupling of W bosons to leptons. Two new experiments [3] aiming at improvements in accuracy by almost one order of magnitude finished data taking and are in the process of extracting $R^{\pi}_{e/\mu}$.

For pions at rest the decay $\pi^+ \to e^+\nu$ is characterized by an electron with $E = \frac{1}{2}m_\pi c^2 = 69.8$ MeV emitted with an exponential time distribution with $\tau_{\pi^+} = 26.0$ ns. Since the 4.2 MeV muon from $\pi^+ \to \mu^+\nu$ at rest travels just $\sim$0.1 g/cm^2 and stays in the π^+ stopping target this decay can be observed through the subsequent decay $\mu^+ \to e^+\nu\bar{\nu}$. The decay chain is characterized by an electron with $E < \frac{1}{2}m_\mu c^2 = 52.8$ MeV emitted with a time distribution first rising with τ_{π^+} and then falling with $\tau_\mu = 2.20$ μs. Ideally, the two decay modes can be perfectly distinguished by the positron energy alone but radiative corrections and imperfections in the experimental setup result in a low-energy tail in the $\pi^+ \to e^+(\gamma)\nu$ positron energy distribution leaking into the region populated by $\pi^+ \to \mu^+\nu$. The uncertainty in this tail fraction is in fact the major source of systematic error in determinations of $R^{\pi}_{e/\mu}$.

TAB. 9.1 – SM predictions and measured values for $R^{\pi}_{e/\mu}$.

	$\Gamma_{\pi^+\to e^+\nu}/\Gamma_{\pi^+\to\mu^+\nu}$	
theory	$1.2353(1) \times 10^{-4}$	[1]
experiment	$1.2312(37) \times 10^{-4}$	[2]

[1] V. Cirigliano and I. Rosell, JHEP **10** (2007) 5.
V. Cirigliano and I. Rosell,
Phys. Rev. Lett. **99** (2007) 231801.

[2] G. Czapek *et al.*, Phys. Rev. Lett. **70** (1993) 17;
D. I. Britton *et al.*, Phys. Rev. Lett. **68** (1992) 3000.

[3] PEN Collaboration, PSI experiment R-05-01 (2005),
D. Počanić and A. van der Schaaf, spokespersons;
PIENU Collaboration, TRIUMF proposal 1072 (2006),
D. Bryman and T. Numao, spokespersons.

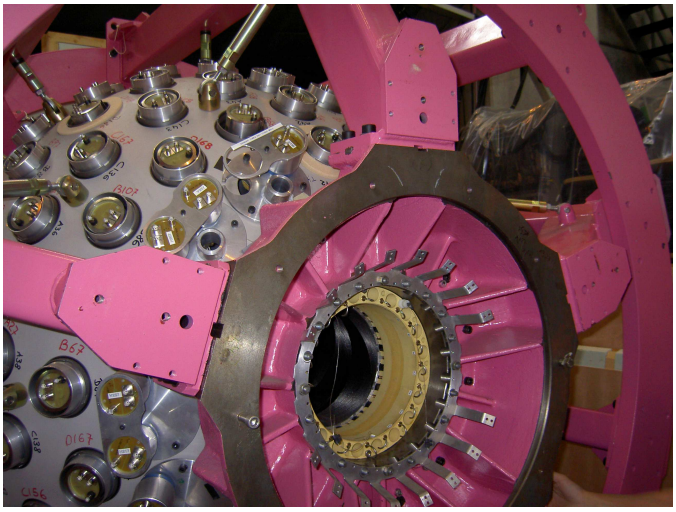

9.1 the PEN experiment

PEN took data at the πE1 beam line at PSI during 2008 – 2010. The most important (and expensive) detector, a 240-element CsI calorimeter shown in Fig. 9.1, was refurbished from the PIBETA experiment [1]. A 75 MeV/c π^+ beam from the πE1 channel was brought to rest in a small plastic scintillator. The beam crossed various scintillators, allowing individual momentum measurements through time-of-flight and dE/dx, and a mini-TPC for tracking.

FIG. 9.1 – The PEN 3π Sr pure-CsI calorimeter before cabling. The carbon-fiber cylinder seen inside the sphere supports the plastic scintillator hodoscope.

These detectors were read both with 2 GS/s waveform digitizers and with 16 μs-range TDC's used to detect preceding beam particles. Secondary particles emitted from the target were tracked in cylindrical MWPC's and crossed a plastic scintillator hodoscope before reaching the calorimeter.

Detector calibrations are done now for all years and reconstruction algorithms have been pushed to perfection. State of the art event simulation all the way down to the data format of the measured events is available but needs some fine-tuning still so detailed studies of the systematic uncertainties haven't started yet.

9.1.1 target waveform analysis

The active target may be called the heart of the detection system since that's where the decays take place and all particles leave their traces. The recorded target waveforms allow a very efficient separation of the two event types of interest in addition to the traditional scheme based on the e^+ energy and the time delay between π^+ stop and e^+ appearance ("decay time"). The procedure is illustrated in Figures 9.2 through 9.4. In a first step the waveform is filtered by folding with a 400-element vector trained to remove all distortions after a few ns (time scale set by the mean scintillator decay time). These distortions are caused by imperfect signal transmission including reflections. In a second step predicted π^+ and e^+ signals are subtracted. These predictions are based on information from almost all detectors but the target itself. The largest uncertainty resides in the prediction of the e^+ signal amplitude which is hampered by Landau fluctuations in the energy loss for given path length (see Fig. 9.3). In a final third step the net waveform is scanned for the appearance of the mono-energetic muon signal by searching for the minimum in the difference in χ^2 for the two hypotheses (see Fig. 9.4). Note that this quantity does not depend on any features of the waveform outside the region of the muon since the difference is zero there.

9.1.2 decay time distributions

The trigger for data readout required a decay positron within a (−30,+220) ns window around the time of an incoming pion. Whereas practically all $\pi \to e\nu$ decays fall within this window, the $\pi \to \mu\nu$, $\mu \to e\nu\bar{\nu}$ decay chain triggers in less than 10% of the cases. Events with positron energies below ∼48 MeV were pre-scaled by 1:64 so the total suppression of the dominant $\pi \to \mu \to e$ chain was three orders of magnitude, which still selects significantly

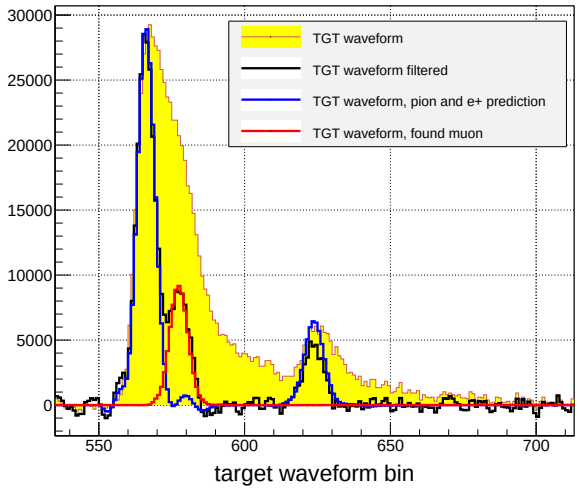

FIG. 9.2 – Target waveform of a $\pi \to \mu \to e$ event before and after waveform filtering. Removal of the predicted pion and positron signals leaves a clean 4 MeV muon signal.

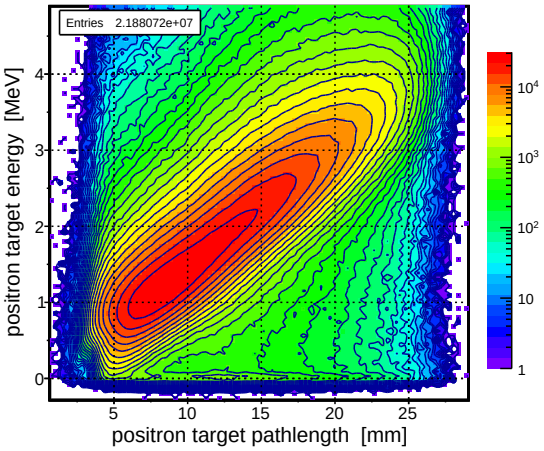

FIG. 9.3 – Observed e^+ target energy vs. reconstructed e^+ path length for events with an isolated e^+ signal. The correlation is exploited in the prediction of e^+ signal in the waveform.

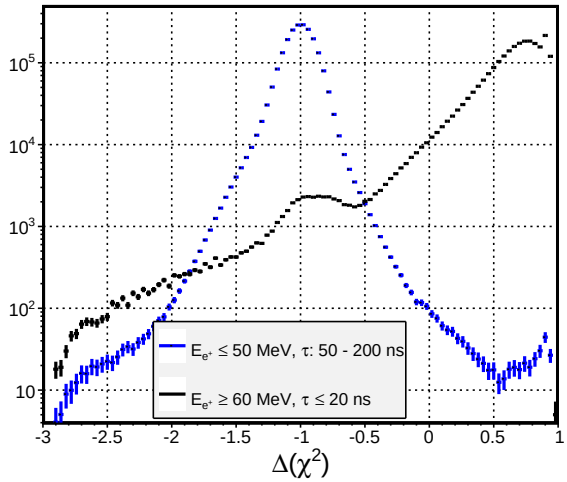

FIG. 9.4 – Distributions of $\Delta(\chi^2)$ (see text) of the target waveform for $\pi \to e$ and for $\pi \to \mu \to e$. The algorithm returns a value within the region shown for any waveform.

more events than in the $\pi \to e$ channel. Fig. 9.5 gives a flavour of the quality of the recorded data. Shown are the decay time distributions of two 2010 event samples enriched in $\pi \to e$ and $\pi \to \mu \to e$, primarily by cuts on e^+ energy and $\Delta(\chi^2)$ of the target waveform. Almost perfect agreement is observed with excursions from expectation below the percent level per 0.5 ns bin.

9.1.3 $\pi \to e\nu\gamma$

When experiments enter new territory, either kinematically or in statistical accuracy, there are often rewards outside the main goal. The "bread and butter" may sometimes even look more interesting for parts of the physics community. As it appears, the PEN data allow for the first time the analysis of the $\pi \to e\nu\gamma$ mode in almost the full phase space. More or less by accident the readout trigger (based on the total CsI energy) selected all $\pi \to e\nu\gamma$ events in the geometric acceptance defined by the CsI calorimeter. Equally important, the target waveform analysis removes any traces of $\mu \to e\nu\bar{\nu}\gamma$ background remaining after a cut on the $e\gamma$ invariant mass (total energy plus total momentum equals pion mass). All background that remains are $\pi \to e\nu$ events in which the e^+ shower is split in two (see below).

The decay $\pi \to e\nu\gamma$ is of interest since, contrary to the inner Bremsstrahlung (IB) contribution, the structure-dependent (SD) contributions are not helicity suppressed and can be extracted from their characteristic kinematic distributions. In the limit $m_e/m_\pi \to 0$:

$$IB(x,y) = \frac{(1-y)((1+(1-x)^2)}{x^2(x+y-1)}$$
$$SD^+(x,y) = (1-x)(x+y-1)^2$$
$$SD^-(x,y) = (1-x)(1-y)^2$$

where x and y are the γ and e^+ energies, respectively, normalized to their maximum value $m_\pi c^2/2$.

By far the best $\pi \to e\nu\gamma$ measurement known in literature was performed by parts of the present PEN collaboration [2]. As explained above, the new PEN data, shown in Fig. 9.6, are much cleaner, even when the total number of events is lower by maybe a factor 2. Much more speculative is the question how well a $\pi \to 3e\nu$ signal can be extracted. This process was studied long ago with the SINDRUM I magnetic spectrometer [3]. PEN accumulated less pion stops but this is more than compensated by the larger acceptance of the non-magnetic setup. At present we refrain from more quantitative statements.

[1] D. Počanić *et al.*, Phys. Rev. Lett. **93** (2004) 181803.

[2] M. Bychkov *et al.*, Phys. Rev. Lett. **103** (2009) 051802.

[3] S. Egli *et al.* (SINDRUM Collaboration), Phys. Lett. **222** (1989) 553.

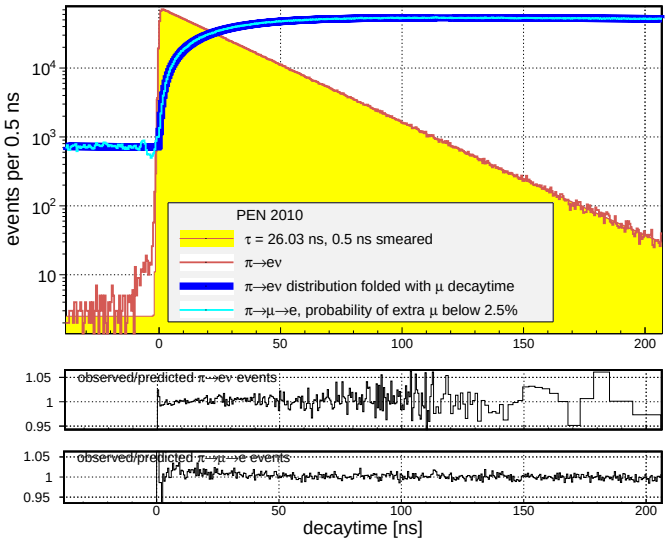

FIG. 9.5 – Histograms of the time delay between incoming π^+ and outgoing e^+. The $\pi \to e\nu$ distribution is perfectly described by the exponential known from literature. The $\pi \to \mu \to e$ distribution is compared with the prediction obtained by folding the observed $\pi \to e\nu$ histogram with the muon decay time distribution. Those who wish to read the branching ratio from this figure should keep in mind that the e^+ energy region below 50 MeV (populated by muon decay) was pre-scaled 1:64 in the readout trigger.

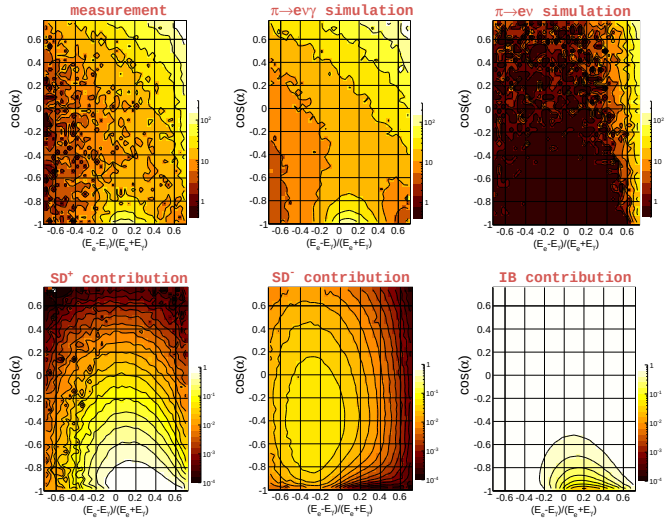

FIG. 9.6 – Kinematic distributions of $\pi \to e\nu\gamma$ (α is the $e^+\gamma$ opening angle). Top row: the distribution from our 2009/10 data (left panel) is compared with the predictions from simulation for signal (middle panel) and $\pi \to e\nu$ background (right panel). 33.140 events are found in the region selected for the figure. Lower row: relative contributions from the two structure-dependent and the inner-Bremsstrahlung contributions in the $\pi \to e\nu\gamma$ simulation. SD^- contributes up to 6%.